ARTICLE

CHRONIC MYELOPROLIFERATIVE NEOPLASMS

CALR-mutated cells are vulnerable to combined inhibition of the proteasome and the endoplasmic reticulum stress response

Jonas S. Jutzi[1], Anna E. Marneth[1], María José Jiménez-Santos[2], Jessica Hem[1], Angel Guerra-Moreno[1], Benjamin Rolles[1], Shruti Bhatt[3,4], Samuel A. Myers[5], Steven A. Carr[6], Yuning Hong[7], Olga Pozdnyakova[8], Peter van Galen[1,6], Fátima Al-Shahrour[2], Anna S. Nam[9] and Ann Mullally[1,3,6]✉

Cancer is driven by somatic mutations that provide a fitness advantage. While targeted therapies often focus on the mutated gene or its direct downstream effectors, imbalances brought on by cell-state alterations may also confer unique vulnerabilities. In myeloproliferative neoplasms (MPN), somatic mutations in the *calreticulin* (*CALR*) gene are disease-initiating through aberrant binding of mutant CALR to the thrombopoietin receptor MPL and ligand-independent activation of JAK-STAT signaling. Despite these mechanistic insights into the pathogenesis of *CALR*-mutant MPN, there are currently no mutant CALR-selective therapies available. Here, we identified differential upregulation of unfolded proteins, the proteasome and the ER stress response in *CALR*-mutant hematopoietic stem cells (HSCs) and megakaryocyte progenitors. We further found that combined pharmacological inhibition of the proteasome and IRE1-XBP1 axis of the ER stress response preferentially targets *Calr*-mutated HSCs and megakaryocytic-lineage cells over wild-type cells in vivo, resulting in an amelioration of the MPN phenotype. In serial transplantation assays following combined proteasome/IRE1 inhibition for six weeks, we did not find preferential depletion of *Calr*-mutant long-term HSCs. Together, these findings leverage altered proteostasis in *Calr*-mutant MPN to identify combinatorial dependencies that may be targeted for therapeutic benefit and suggest that eradicating disease-propagating *Calr*-mutant LT-HSCs may require more sustained treatment.

Leukemia (2023) 37:359–369; https://doi.org/10.1038/s41375-022-01781-0

INTRODUCTION

Myeloproliferative neoplasms (MPN) comprise chronic bone marrow (BM) cancers, due to the acquisition of MPN driver mutations arising in the hematopoietic stem cell (HSC) compartment [1]. MPN phenotypic driver mutations occur in *JAK2*, *CALR* or *MPL*, typically in a mutually exclusive manner, and all lead to constitutively active JAK-STAT signaling. *CALR* mutations are found in patients with the MPN subtypes Essential Thrombocytosis (ET) and myelofibrosis (MF) and are detectable in 20–25% of all MPN patients [2, 3]. Next-generation sequencing studies in patients [4] and multiple mutant CALR MPN mouse models have shown that *CALR* mutations alone are sufficient to cause MPN [5–7].

CALR is an endoplasmic reticulum (ER) chaperone aiding the quality control of newly synthesized proteins. Mutant CALR, however, gains a novel mutant-specific C-terminus resulting from frameshift mutations, caused by either deletion (Type I) or insertion (Type II) mutations [2, 3]. Of these mutations, a 52-base pair (bp) deletion ($CALR^{\Delta 52}$) is the most frequent [2, 3, 8]. The underlying disease-initiating mechanism involves the binding of the mutated CALR protein to the thrombopoietin receptor MPL, and constitutive activation of downstream JAK-STAT signaling [5]. MPL is mainly expressed on HSCs and megakaryocytes, hence these cell populations are predominantly affected by the *CALR* mutation. Mutant CALR-MPL signaling leads to clonal expansion and increased megakaryopoiesis, resulting in elevated platelet counts and sometimes subsequent development of MF, as recapitulated in a mutant $Calr^{\Delta 52}$ knockin mouse model [7].

Another key function of the wild-type CALR protein is to maintain ER calcium homeostasis through the predominantly negatively charged C-terminus. The C-terminus of the mutant CALR protein does not harbor the ER retention signal ("KDEL") and its amino acid composition changes from a predominantly negative to a positive charge [2, 3]. These changes in amino acid composition interfere with the ability of mutant CALR to retain

[1]Division of Hematology, Department of Medicine, Brigham and Women's Hospital, Harvard Medical School, Boston, MA, USA. [2]Bioinformatics Unit, Structural Biology Programme, Spanish National Cancer Research Centre (CNIO), Madrid, Spain. [3]Department of Medical Oncology, Dana-Farber Cancer Institute, Boston, MA, USA. [4]Department of Pharmacy, National University of Singapore, Singapore, Singapore. [5]Center for Autoimmunity and Inflammation, La Jolla Institute for Immunology, La Jolla, CA 92037, USA. [6]The Broad Institute of MIT and Harvard, Cambridge, MA, USA. [7]Department of Chemistry and Physics, La Trobe Institute for Molecular Science, La Trobe University, Melbourne, VIC 3083, Australia. [8]Department of Pathology, Brigham and Women's Hospital, Harvard Medical School, Boston, MA, USA. [9]Weill Cornell Medicine, New York City, N.Y., USA. ✉email: ann_mullally@dfci.harvard.edu

Received: 16 June 2022 Revised: 21 November 2022 Accepted: 25 November 2022
Published online: 6 December 2022

calcium within the ER [8]. A recent study demonstrated that impaired ER calcium retention in Type I *CALR* mutations results in the induction of the IRE1-XBP1 branch of the unfolded protein response (UPR) [9]. When activated, inositol-requiring enzyme 1 a (IRE1a) splices a 26-nucleotide sequence from an intron of cytosolic *XBP1u* transcripts resulting in translation of the XBP1 transcription factor, which promotes the transcription of protein folding genes [10–12]. We have previously reported activation of the IRE1a-XBP1 branch of the UPR in primary samples obtained from patients with *CALR*-mutated MPN [13].

The UPR is a cellular mechanism to cope with ER stress induced by misfolded proteins [14–16]. There are three main ways by which the UPR responds to ER stress [14–16]. Firstly, by increasing the protein folding capacity of the ER through transcriptional induction of chaperones. Secondly, by attenuating global protein translation, which decreases the input of newly synthesized and not yet folded proteins into the ER. And thirdly, the ER can shuttle misfolded proteins back to the cytosol, where they get ubiquitinylated and degraded by the proteasome. The latter process is called ER-associated protein degradation (ERAD) and is key in alleviating ER stress. If the ER stress persists or reaches a critical overload, terminal UPR is activated, leading to apoptosis [17, 18].

Here, using mutant *Calr* knockin mice and primary *CALR*-mutant MPN samples, we find differential upregulation of the IRE1a-XBP1 axis of the UPR as well as the proteasome in CALR-mutated hematopoietic stem cells (HSCs) and megakaryocytes. Using isogenic cell lines, functional genomics and pharmacological inhibitor studies, we identify these pathways as genetic and therapeutic vulnerabilities in mutant CALR-transformed hematopoietic cells. Finally, we show that combined inhibition of the proteasome and IRE1a preferentially targets *Calr*-mutant cells in vivo, resulting in amelioration of MPN features in mutant CALR knockin mice.

MATERIALS AND METHODS

Megakaryocyte differentiation and enrichment for quantitative proteomics

Unfractionated BM cells of eight-week-old mice were placed into culture at a concentration of 1-10*10^6 cells/mL in DMEM supplemented with 10% FBS, 1% penicillin/streptomycin, and 50 ng/mL TPO (Peprotech, cat. no. 315-14), in 10 cm dishes and cultured for 4–5 days until large megakaryocytes were visible under the microscope. Cells were harvested by gently washing them with pre-warmed PBS. Cells were transferred into 50 mL conical tubes. After spin down (200 g, 5 min, room temperature), supernatant was removed, and the pellet resuspended in 1 mL PBS and subjected to BSA gradients. In brief, in 15 mL conical tubes, 1 mL of 3% BSA was gently overlayed with 1 mL 1.5% BSA, followed by 1 mL of the cells. The cells were allowed to move along the gradient for 30 min. The supernatant was carefully removed, and the bottom layer gently washed three times with PBS (200 g, 5 min, room temperature). The pellet was resuspended in 1 mL PBS and the gradient performed a second time to increase the purity. After the last wash, cells were pelleted, supernatant removed, and pellets stored at −20 °C until further processing. Quantitative proteomics was performed using a previously published protocol [19].

Experimental details of generation of BA/F3 cell lines, BA/F3 cell proliferation assays, chemical screen, CALR mice, complete blood cell count analysis, competitive BM transplant, in vivo treatments, stem and progenitor cell analysis, intracellular XBP1s flow cytometry, detection of misfolded proteins, morphologic histopathological analysis, western blot, RNA isolation, BH3 profiling, Genotyping of Transcriptomes (GoT), bioinformatic and statistical analyses are described in supplementary methods.

RESULTS

The IRE1a-XBP1 axis of the unfolded protein response and the proteasome are upregulated in CALR-mutant stem cells, megakaryocyte progenitors, and megakaryocytes

To identify genes and pathways that are differentially expressed in $CALR^{\Delta 52}$ cells, we first performed RNA-sequencing (RNA-seq) on sorted long-term hematopoietic stem cells (LT-HSCs) from $Calr^{\Delta 52/\Delta 52}$ and $Calr^{+/+}$ knockin mice (Fig. 1, Supplementary Fig. 1). We found that *Xbp1*, a key downstream transcription factor in the IRE1a branch [20] of the UPR was upregulated in mutant *Calr* LT-HSCs as compared with wild-type LT-HSCs (Fig. 1A). Since functional *Xbp1* is formed through cytosolic splicing of unspliced *Xbp1* (*Xbp1u*) into *Xbp1* spliced (*Xbp1s*) by IRE1a, we next assessed *Xbp1u* and *Xbp1s* levels versus *Xbp1u* levels, as the gold standard of Xbp1-mediated UPR activation. Further analysis of the RNA-seq data revealed that not only *Xbp1u* was increased in mutant *Calr* cells as compared to wild-type cells, but also *Xbp1s* as well as the ratio of spliced to unspliced *Xbp1* transcripts (Fig. 1A, *right panel*). To confirm the upregulation of the XBP1s at the protein level in a more disease-relevant model, we next assessed XBP1s protein in heterozygous mutant $Calr^{\Delta 52}$ knockin mice. To do so, we performed intracellular XBP1s flow cytometry staining of $Calr^{\Delta 52/+}$ VAVCre and $Calr^{+/+}$ VAVCre control hematopoietic stem and progenitor cells (HSPCs) (Fig. 1B). We found XBP1s to be increased in $Calr^{\Delta 52/+}$ VAVCre animals as compared to controls (Fig. 1B, Supplementary Fig. 1A). XBP1s levels further increased in HSPCs isolated from $Calr^{\Delta 52/+}$ VAVCre and $Calr^{+/+}$ VAVCre mice upon ex vivo treatment with thapsigargin (TG), a pharmacological inducer of UPR through ER calcium depletion (Fig. 1B, Supplementary Fig. 1A). Further analyzing the LT-HSC RNA-seq data, we next performed gene-set enrichment analysis (GSEA). We found the "proteasome" (KEGG) pathway to be amongst the most differentially upregulated pathways in *Calr*-mutant LT-HSCs as compared to control cells (Fig. 1C), suggesting a second mechanism by which *Calr*-mutated cells alleviate ER stress. Since megakaryopoiesis is increased and aberrant in *CALR*-mutant MPN, we next focused on this key disease-relevant population and performed quantitative proteomics on ex vivo differentiated megakaryocytes (Fig. 1D, Supplementary Fig. 1). We captured a total of 2640 proteins, of which 282 were significantly more abundant in *Calr*-mutant megakaryocytes as compared to wild-type control megakaryocytes (Fig. 1D). Amongst the most differentially abundant proteins in *Calr*-mutant megakaryocytes, we identified 12 proteins linked to ER chaperone activity and 12 subunits of the 26 s proteasome, aligning with our RNA-seq data on mouse LT-HSCs. Of note, CALR mutant protein was significantly less abundant in *Calr*-mutant megakaryocytes as compared to wild-type megakaryocytes (Fig. 1D), consistent with previous reports showing instability and decreased levels of the mutant CALR protein in mouse cells [21].

To expand our analysis to human cells, we analyzed our published GoT data set on human *CALR*-mutated HSPCs [13]. We found that the KEGG pathway "proteasome" was significantly enriched in *CALR*-mutated megakaryocyte progenitors (MkPs) as well as HSPCs, as compared to wild-type MkPs and HSPCs (Fig. 1E). Furthermore, the proteasome and the XBP1 expression modules positively correlated in *CALR*-mutated HSPCs and MkPs but not in wild-type cells from the same patients (Fig. 1F), consistent with these pathways being activated in concert in *CALR*-mutated MPN cells.

IRE1a, ERAD, and the proteasome are required for mutant CALR-driven transformation of hematopoietic cells

Next, we aimed to determine whether upregulation of the UPR and the proteasome represents a mechanism by which *CALR*-mutant cells cope with ER stress and to assess if inhibition of either pathway represents a therapeutic vulnerability in *CALR*-mutant cells. We first addressed this question using functional genomics and performed a whole-genome CRISPR knockout depletion screen in mutant CALR-transformed BA/F3-MPL cells (full details of the whole-genome CRISPR screen are described separately) [22]. We performed GSEA to identify pathways that were differentially depleted in $CALR^{\Delta 52}$-transformed cells as compared to empty vector (EV) control cells. We have previously

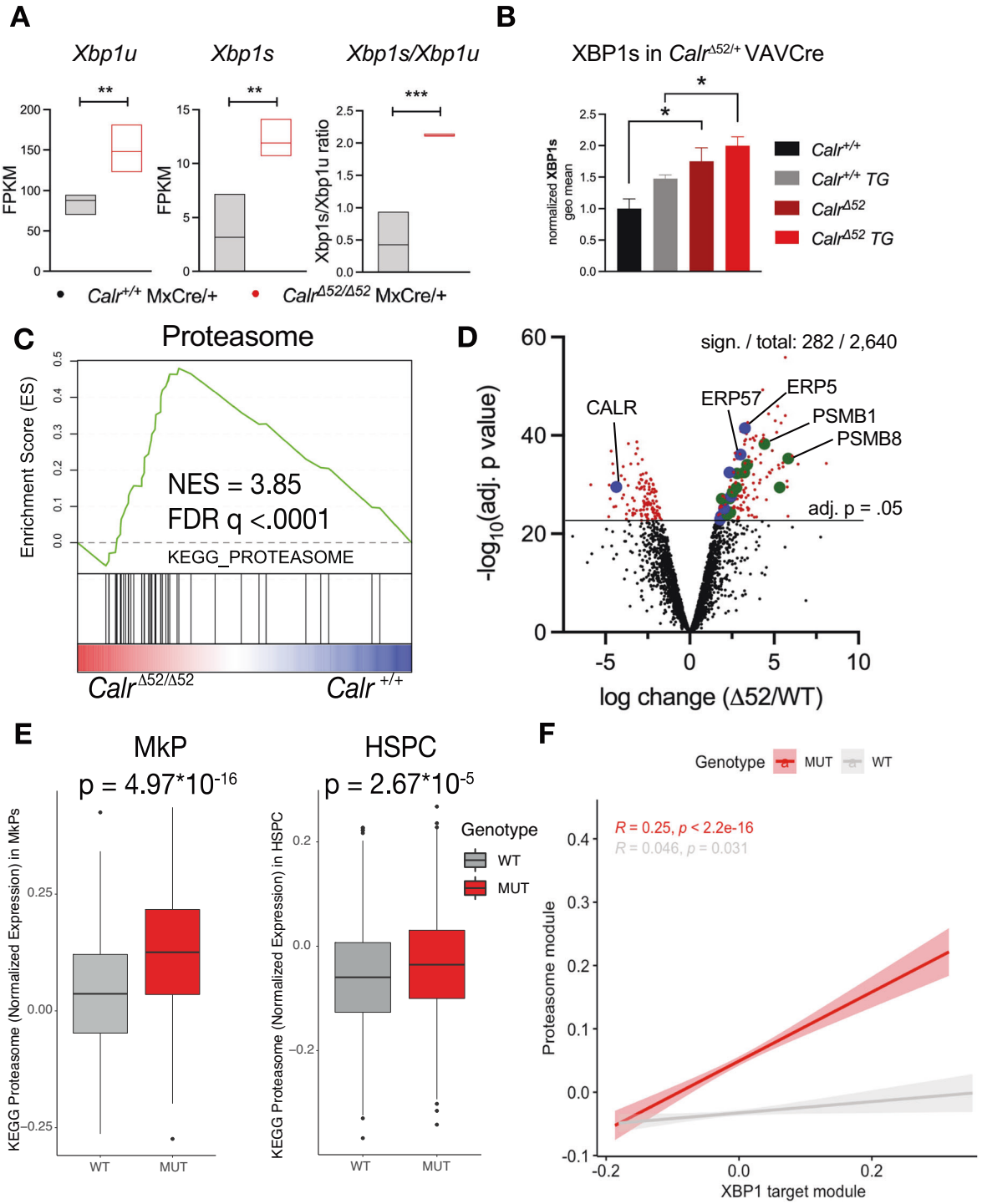

Fig. 1 The IRE1a-XBP1 axis of the unfolded protein response and the proteasome are upregulated in CALR$^{\Delta 52}$ stem cells. A *Xbp1u* (left), *Xbp1s* (middle), and *Xbp1s/Xbp1u* ratio in long-term hematopoietic stem cells (LT-HSCs). FPKM: Fragments Per Kilobase of transcript per Million mapped reads. $n = 3$–4 mice/genotype. **B** In vivo spliced XBP1s protein levels, determined by flow cytometry in *Calr*$^{\Delta 52/+}$ VAVCre versus *Calr*$^{+/+}$ VAVCre control bone marrow single cells, either untreated or treated with the unfolded protein response-inducer thapsigargin (TG). $n = 3$–4 mice/genotype and group. Mean ± SEM. Statistical analysis performed using One-way ANOVA, $^*p < 0.05$. **C** Gene-set enrichment analyses (GSEA) depicting a significant enrichment of the KEGG proteasome pathway in *Calr*$^{\Delta 52/\Delta 52}$ versus *Calr*$^{+/+}$ LT-HSCs. $n = 3$–4 mice/genotype. **D** Quantitative proteomics, performed on ex vivo cultured CALR$^{+/+}$ and CALR$^{\Delta 52/\Delta 52}$ megakaryocyte proteins. $n = 3$ per genotype. Volcano plot showing log-fold change and $\log_{10}$ adjusted *p* values of $n = 2640$ total captured peptides. Statistically significantly differentially expressed proteins are highlighted in red. Important differentially expressed ER chaperones are highlighted in blue, proteasome proteins are highlighted in green. **E** Expression of KEGG proteasome pathway expression in megakaryocyte progenitors (MkP, left) and hematopoietic stem and progenitor cells (HSPCs) (right). $n = 454$ wild-type versus $n = 648$ *CALR*-mutant HSPCs and $n = 1724$ wild-type versus $n = 621$ *CALR*-mutant MkPs from $n = 5$ patients with Essential Thrombocythemia (ET). Statistical analysis performed using likelihood ratio tests of linear mixed model with/without mutation status. **F** Pearson correlation of the expression of XBP1 target (Reactome) and the proteasome (KEGG) gene sets in *CALR* wild-type (gray) and *CALR* mutant (red) HSPCs and MkPs from (**E**).

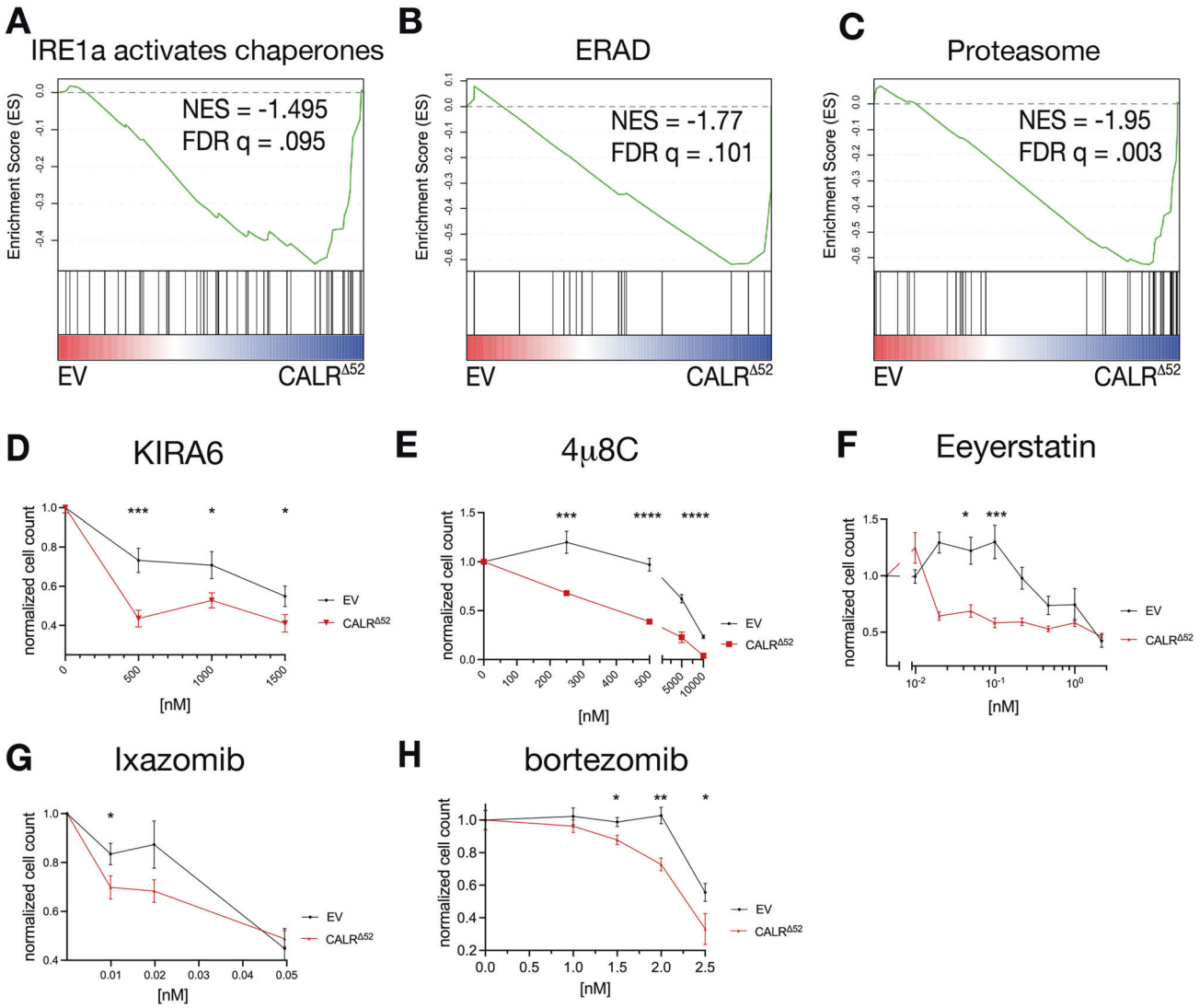

Fig. 2 CALR$^{\Delta 52}$ cells are differentially vulnerable to depletion of the proteasome and UPR-associated pathways. A–C GSEA on the whole-genome CRISPR depletion screen [22] hits depicting the Reactome pathway "IRE1a activates chaperone" (**A**), the BIOCARTA pathway "ERAD" (**B**), and the KEGG pathway "Proteasome" (**C**) as significantly depleted in CALR$^{\Delta 52}$ -IL3 versus empty vector +IL3 cells. **D–G** Live cell count was determined 72 h after drug administration by flow cytometry in EV- and CALR$^{\Delta 52}$-expressing BA/F3-MPL cells at stated concentrations and cultured in the presence or absence of IL3, respectively. Two-sided Student's *t* tests were performed at concentrations as indicated, comparing EV with CALR$^{\Delta 52}$. *$p < 0.05$, **$p < 0.01$, ***$p < 0.001$. $n = 3$ experiments, performed in triplicates. Mean ± SEM. Growth curve after KIRA6 (**D**), 4μ8C (**E**), Eeyerstatin, and Ixazomib administration, normalized to DMSO controls. **H** Growth curves of BA/F3-MPL-EV or -CALR$^{\Delta 52}$-expressing cells in the presence or absence of IL3, respectively, treated with either DMSO or bortezomib at concentrations indicated, and normalized to DMSO control for each cell line. Two-sided Student's *t* tests were performed at 1.5 nM, 2.0 nM, and 2.5 nM concentrations as indicated. *$p < 0.05$, **$p < 0.01$.

reported that we found the "UPR" pathway (Hallmark) (FDR $q = 0.014$) to be differentially depleted in CALR$^{\Delta 52}$-transformed cells as compared to EV cells [22]. Here, in additional analyses, we found similar findings for the "IRE1a activates chaperones" (Reactome) (FDR $q = 0.095$), the ERAD (FDR $q = 0.101$) (BIOCARTA), and the "Proteasome" (KEGG) pathways (FDR $q = 0.003$). (Fig. 2A–C).

Having shown a differential genetic dependency on the UPR and proteasome pathways in mutant CALR-transformed cells, we next tested pharmacological inhibition of IRE1-XBP1s, ERAD, and the proteasome in vitro. Upon treatment with the IRE1 inhibitors KIRA6 and 4μ8C (Fig. 2D+E), the ERAD inhibitor Eyerstatin (Fig. 2F), and the proteasome inhibitor ixazomib (Fig. 2G), we observed a significant reduction in growth of mutant CALR$^{\Delta 52}$-transformed BA/F3-MPL cells as compared to EV control cells. In addition, CALR$^{\Delta 52}$ cells also showed a significantly increased sensitivity to the proteasome inhibitor, bortezomib as compared to control cells (Fig. 2H).

Inhibition of the proteasome leads to an accumulation of misfolded proteins, resulting in pro-apoptotic priming and reduced platelet count in vivo

As bortezomib is in clinical use for the treatment of other diseases, we further interrogated the use of this proteosome inhibitor ex vivo and in vivo. We hypothesized that proteasomal inhibition differentially promotes terminal UPR in mutant CALR-expressing cells as compared with wild-type cells, resulting in apoptosis. To investigate this, we differentiated BM into megakaryocytes ex vivo, treated with either DMSO or bortezomib, stained with megakaryocytic surface expression markers, and subjected these cells to BH3 profiling [23]. Bortezomib-treated *Calr*$^{\Delta 52/+}$ megakaryocytes showed increased priming for the pro-apoptotic BIM

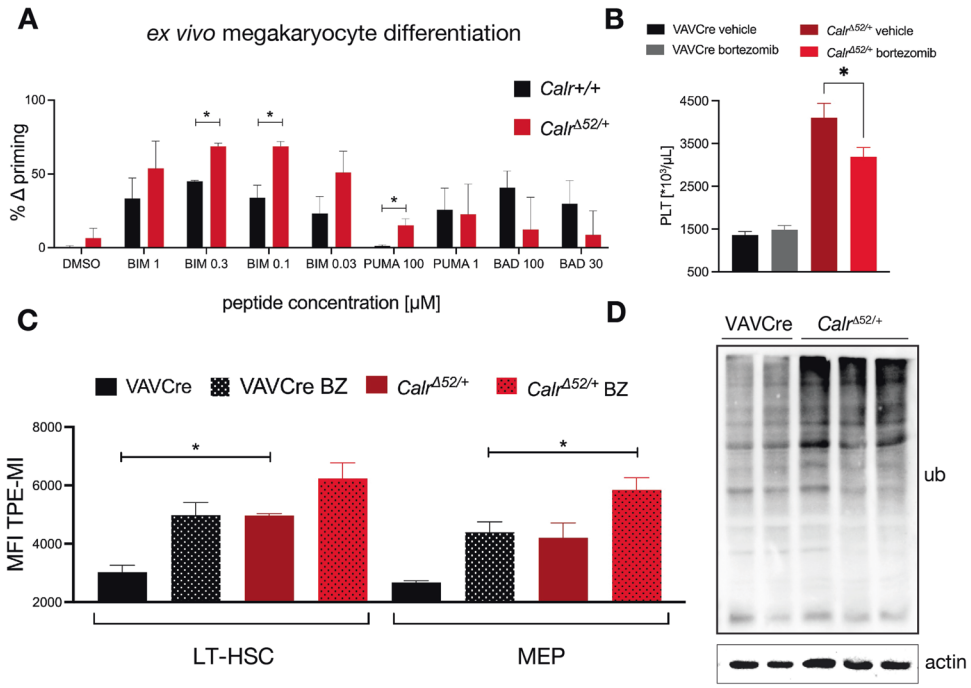

Fig. 3 Treatment with the proteasome inhibitor bortezomib induces apoptotic priming and decreases platelet counts in *Calr*$^{\Delta 52/+}$ mice. **A** BH3 profiling in *Calr*$^{+/+}$ and *Calr*$^{\Delta 52/+}$ primary mouse megakaryocytes following ex vivo treatment with bortezomib (10 nM) for 16 h, showing significantly increased priming to pro-apoptotic BIM peptides (0.3 mM and 0.1 mM) in *Calr*$^{\Delta 52/+}$. $n = 3$ mice/group. Mean ± SEM. *$p < 0.05$. **B** Platelet values of primary *Calr*$^{\Delta 52/+}$ VAVCre and *Calr*$^{+/+}$ VAVCre control mice, following five weeks of treatment with either vehicle or bortezomib. $n = 6$–7 mice/genotype and condition. One-Way ANOVA. Mean ± SEM. *$p < 0.05$. **C** Quantification of misfolded proteins by flow cytometry in HSPCs of *Calr*$^{\Delta 52/+}$ VAVCre and VAVCre control mice treated with bortezomib (1 mg/kg body weight) for 16 hours. $n = 3$–4 per genotype. Mean ± SEM. MFI: mean fluorescence intensity, LSK: lin- kit$^+$ sca-1$^+$, LK: lin$^-$ kit$^+$, LT-HSC: long-term hematopoietic stem cells, TPE-MI: tetraphenylethene maleimide. $n = 3$–4. **D** Quantification of ubiquitinylated proteins by western blotting on *Calr*$^{\Delta 52/+}$ VAVCre and VAVCre control BM treated with bortezomib (10 nM) ex vivo for 4 hours.

and PUMA peptides as compared to wild-type bortezomib-treated megakaryocytes (Fig. 3A). To test if this differential priming represents an in vivo vulnerability, we next treated primary *Calr*$^{\Delta 52/+}$ VAVCre and *Calr*$^{+/+}$ VAVCre control mice with bortezomib for five weeks. We found a significant reduction in platelet counts in bortezomib-treated *Calr*$^{\Delta 52/+}$ VAVCre mice but not in bortezomib-treated *Calr*$^{+/+}$ VAVCre animals (Fig. 3B). We hypothesized that the findings we observed with ex vivo and in vivo bortezomib treatment were a consequence of increased accumulation of misfolded and poly-ubiquitinylated proteins in *Calr*$^{\Delta 52/+}$ cells. To assess the abundance of misfolded proteins in vivo we used TPE-MI, a molecule that binds accessible cysteines that are present in un- or misfolded proteins but normally concealed in properly folded proteins [24]. In *Calr*$^{\Delta 52/+}$ mice treated with bortezomib, we found a significantly elevated level of misfolded proteins by flow cytometry in megakaryocyte-erythrocyte progenitors (MEPs) as well as long-term HSCs (LT-HSCs), as compared to *Calr*$^{+/+}$ mice treated with bortezomib (Fig. 3C) [24]. Finally, we found that bortezomib-treated *Calr*$^{\Delta 52/+}$ VAVCre unfractionated BM showed higher levels of poly-ubiquitinylated proteins as compared to bortezomib-treated *Calr*$^{+/+}$ VAVCre BM (Fig. 3D).

We next wanted to determine whether proteasome inhibition preferentially affects mutant over wild-type cells in a chimeric mouse model, which allows us to simultaneously assess the therapy effects on *Calr*$^{\Delta 52/+}$ and *Calr*$^{+/+}$ cells within the same mouse. For this, we crossed *Calr*$^{\Delta 52/+}$ MxCre mice with UBC-GFP mice. These mice express GFP in all tissues, including CD45-negative platelets, which allowed us to track platelet chimerism by flow cytometry. We transplanted an equal amount of BM of *Calr*$^{\Delta 52/+}$ MxCre UBC-GFP and CD45.1$^+$ competitor into lethally irradiated recipient mice (Fig. 4A). We observed a significant reduction in *Calr*$^{\Delta 52}$ mutant myeloid cell chimerism in bortezomib-treated mice with non-significant changes in white blood cell counts (WBC) (Fig. 4B+C). Further, platelet chimerism as determined by GFP expression was significantly decreased in bortezomib-treated mice while platelet values were not reduced upon treatment, suggesting that bortezomib alone may not be sufficient for ameliorating the disease (Fig. 4D+E). The hematocrit remained unchanged over time (Supplementary Fig. 2A). In the BM, the *Calr*$^{\Delta 52/+}$ GFP$^+$ mutant percentage in CD11b$^+$ Gr-1$^+$ myeloid cells was significantly decreased (Fig. 4F). Although the overall frequency of megakaryocyte-erythrocyte progenitors (MEP) was unchanged, the frequency of *Calr*$^{\Delta 52/+}$ GFP$^+$ mutant MEPs was significantly decreased upon treatment with bortezomib (Fig. 4G). Similarly, the frequency of *Calr*$^{\Delta 52/+}$ GFP$^+$ MkP was significantly decreased while other myeloid progenitors remained unchanged (Supplementary Fig. 2B–E).These data indicate that although proteasome inhibition showed selectivity toward *Calr*$^{\Delta 52/+}$ megakaryocytic cells, single-agent bortezomib did not induce hematological responses.

Combined inhibition of IRE1a and the proteasome reduces MPN-related hematopoietic progenitors in mutant *Calr* mice in vivo

While bortezomib reduced *Calr*-mutant cells in mice, this effect was relatively mild and MEP as well as platelet values remained unchanged. We hypothesized that combined inhibition of the proteasome and IRE1a-XBP1 pathways would lead to more robust UPR-induced apoptosis preferentially in *Calr*-mutant cells. First, we tested increasing doses of the IRE1a inhibitor KIRA6, alone or in combination with bortezomib in BA/F3-MPL-EV an -CALR$^{\Delta 52}$ cells (Fig. 5A–D). We found that a low dose of either KIRA6 or bortezomib alone did not impair the growth of control cells, but significantly reduced growth in CALR$^{\Delta 52}$ cells. This growth

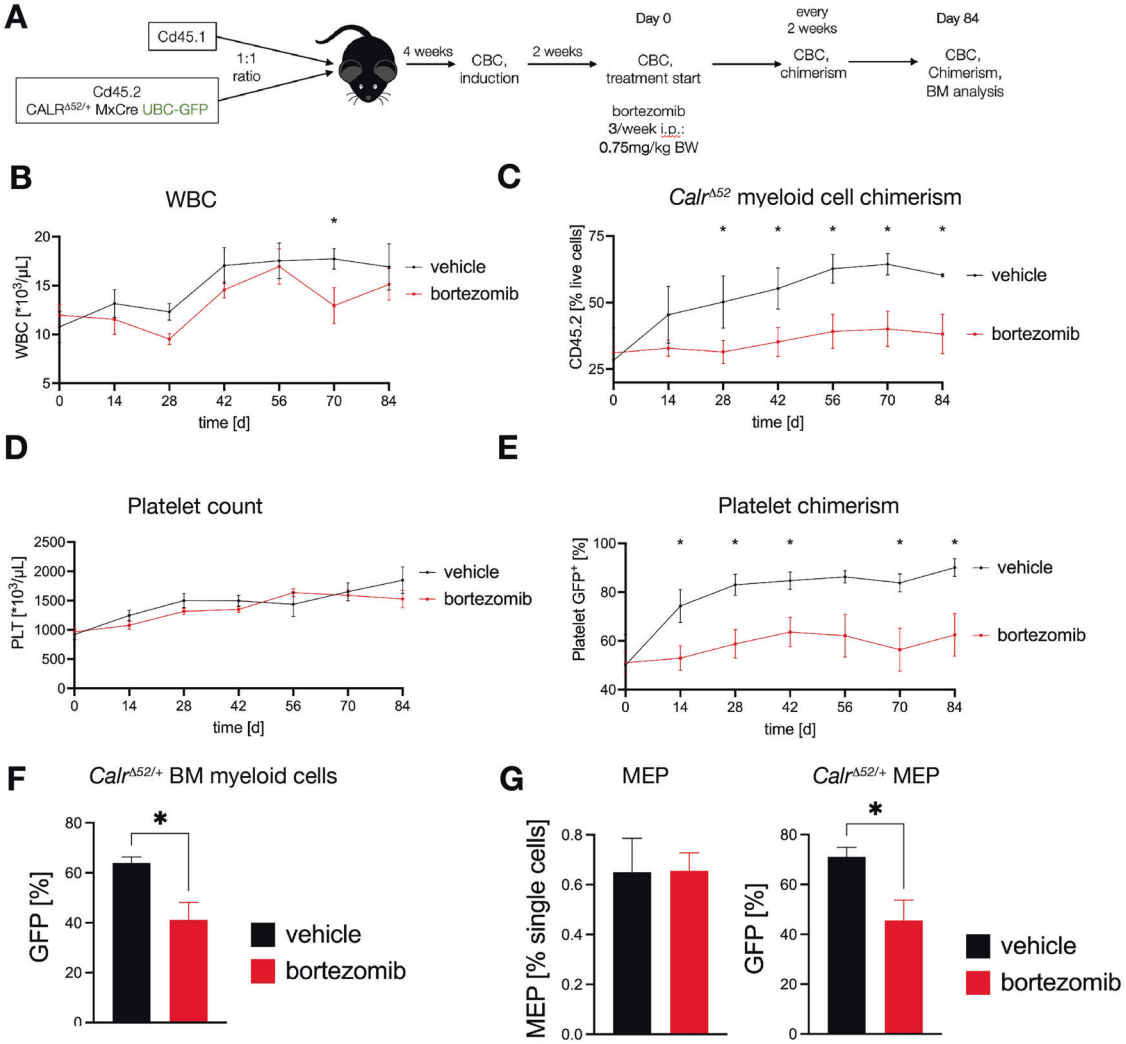

Fig. 4 *Calr*$^{\Delta 52/+}$ myeloid cells are sensitive to the inhibition of the proteasome in chimeric mice treated with bortezomib. A–G Chimeric *Calr*$^{\Delta 52/+}$ MxCre UBC-GFP mice treated with either vehicle or bortezomib. $n = 4$–6 mice/condition. $n = 2$ donor mice/genotype in two independent experiments. Mean ± SEM. *$p < 0.05$ (**A**) Schematic overview of chimeric transplantation experiment. CD45.1$^+$ competitor bone marrow (BM) BM cells were mixed in a 1:1 ratio with CD45.2$^+$ *Calr*$^{\Delta 52/+}$ MxCre UBC-GFP BM and transplanted into lethally irradiated CD45.1$^+$ recipient animals. Four weeks after transplantation complete blood cell counts (CBC) were obtained and pI:pC induction started. Treatment was started 2 weeks later and CBCs were obtained every two weeks. **B** White blood cell count (WBC) of vehicle- and bortezomib-treated chimeric mice over time. **C** CD45.2$^+$ *Calr* mutant cell percentage in CD11b$^+$ Gr-1$^+$ myeloid peripheral blood cells, obtained by flow cytometry of vehicle- and bortezomib-treated chimeric mice over time. **D** Platelet counts and (**E**) Platelet chimerism of vehicle- and bortezomib-treated chimeric mice over time. **F** *Calr*$^{\Delta 52/+}$ GFP$^+$ mutant percentage in CD11b$^+$ Gr-1$^+$ myeloid cells in the BM. **G** Frequency of megakaryocyte-erythrocyte progenitors (MEP) (left) and frequency of GFP$^+$ *Calr*$^{\Delta 52/+}$ GFP$^+$ mutant MEP (right).

reduction was further accentuated when the two drugs were combined (Fig. 5B). We found that KIRA6 and bortezomib synergistically reduced the growth of transformed CALR$^{\Delta 52}$ but not EV cells (Fig. 5C+D). To translate this to a more clinically applicable model, we treated primary heterozygous *Calr*$^{\Delta 52/+}$ VAVCre and VAVCre control mice with either vehicle, bortezomib, KIRA6, or KIRA6 plus bortezomib for five weeks (Fig. 5E–H). Platelets in KIRA6-treated *Calr*-mutant mice were not significantly reduced, while platelets were significantly reduced in bortezomib and KIRA6 plus bortezomib-treated mice (Fig. 5E). No changes in platelet counts were observed in VAVCre control mice (Fig. 5E). There was no observed toxicity, and no other peripheral blood cell type was significantly affected by either treatment (Supplementary Fig. 3A+B). The frequencies of SLAM$^+$ LT-HSCs as well as MkPs were significantly reduced in KIRA6 plus bortezomib-treated *Calr*-mutant mice but not in wild-type mice (Fig. 5F+G). To determine the mechanism behind this effect, we measured caspase 3/7 level in stem and progenitor cells of treated mice and found increased apoptosis in KIRA6 plus bortezomib-treated *Calr*-mutant LT-HSCs (Fig. 5H). To compare the effect of targeting the UPR and the proteasome to ruxolitinib, we treated *Calr*$^{\Delta 52/+}$ VAVCre primary mice with either vehicle, bortezomib, KIRA6, KIRA6 plus bortezomib, or ruxolitinib (Supplementary Fig. 4). As seen in preclinical *Jak2*^{V617F} mouse models treated with ruxolitinib [25], we found a decrease in WBC in treated mice with no changes in platelet counts, hematocrit, or body weight (Supplementary Fig. 4A–C). In comparison, platelets and MkPs were significantly decreased in KIRA6 plus bortezomib-treated animals as a result of increased caspase 3/7 in MEPs (Supplementary Fig. 4B, D–G).

Combined inhibition of IRE1a and the proteasome preferentially targets mutant CALR cells and ameliorates MPN-relevant features

Encouraged by the preferential killing of *Calr*$^{\Delta 52}$ cells in primary *Calr*$^{\Delta 52}$ mice treated with KIRA6 plus bortezomib as well as the

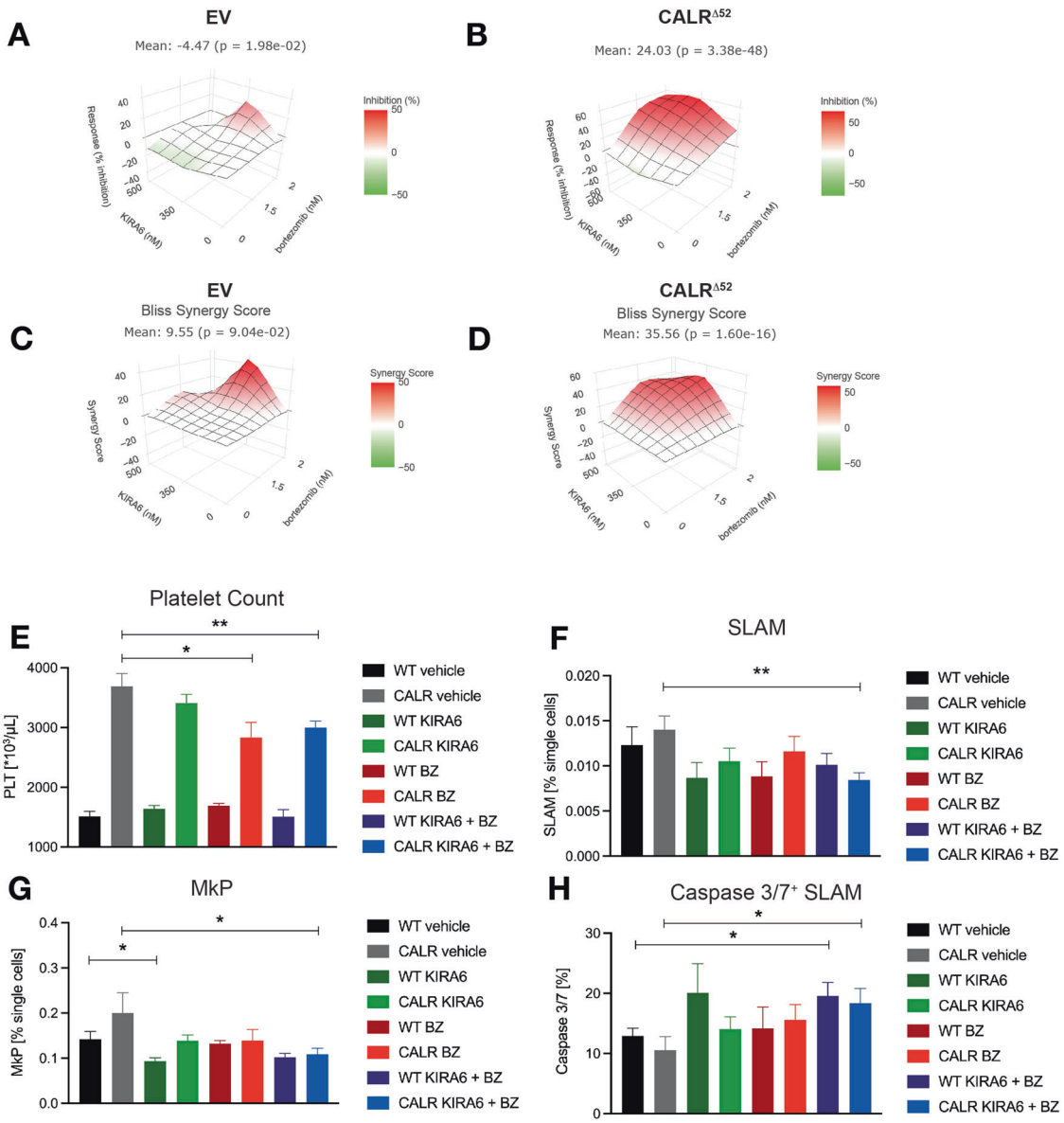

Fig. 5 Combined proteasomal and IRE1a inhibition synergizes in killing CALR$^{\Delta 52}$ mutant cells. A + B Percent growth inhibition of BA/F3-MPL-EV (**A**) or -CALR$^{\Delta 52}$ (**B**) expressing cells at 72 hours of treatment with indicated KIRA6 and/or bortezomib doses, in the presence or absence of IL3, respectively. **C + D** Bliss Synergy score calculated using SynergyFinder [38] based on the growth inhibition from (**A + B**) for EV (**C**) and CALR$^{\Delta 52}$ (**D**) cells treated with various combinations of KIRA6 and bortezomib. A mean Bliss score >10 with a p value < 0.05 indicates synergy between drugs. **E–H** Analyses of *Calr*$^{\Delta 52/+}$ VAVCre or VAVCre control mice treated with either KIRA6, bortezomib (BZ), or the combination of both for five weeks. $n = 5$–8 per group and genotype. Mean ± SEM. *$p < 0.05$, **$p < 0.01$. **E** Platelet values of *Calr*$^{\Delta 52/+}$ VAVCre and VAVCre control mice. **F** Long-term hematopoietic stem cells frequency (LT-HSC) frequency (SLAM) of single bone marrow (BM) cells of treated *Calr*$^{\Delta 52/+}$ VAVCre and VAVCre control mice. **G** Megakaryocyte-erythroid progenitor (MEP) frequency single BM cells in treated *Calr*$^{\Delta 52/+}$ VAVCre and VAVCre control mice. **H** Percentage of caspase 3/7 positive SLAM-positive stem cells of treated *Calr*$^{\Delta 52/+}$ VAVCre and VAVCre control mice.

lack of overt toxicity, we tested whether combined inhibition of IRE1a and the proteasome preferentially targets mutant CALR-expressing stem cells. To test this, we used the same chimeric transplantation model as before by transplanting *Calr*$^{\Delta 52/+}$ MxCre UBC-GFP and CD45.1^{+} competitor into lethally irradiated recipient mice (Fig. 4A). At the start of the treatment (day 0) following engraftment and pIpC induction, mice were randomized according to the same parameters as described for the use of bortezomib in chimeric mice and subjected to treatment with either vehicle, KIRA6, bortezomib, or KIRA6 plus bortezomib for 42 days (Fig. 6). We found a significant reduction in platelets in KIRA6 plus bortezomib-treated mice over time, while the platelet counts in mice treated with KIRA6 or bortezomib were not significantly different from vehicle control mice (Fig. 6A). Platelet chimerism was significantly reduced in combined treated mice at the six-week time point (76.5% vehicle versus 66.6% KIRA6 + bortezomib) (Fig. 6B). We further observed that the fraction of GFP^{+} cells within the *Calr*-mutant lineage^{-} sca-1^{+} kit^{+} (LSK) progenitor compartment was significantly reduced in combined treated mice compared to vehicle (Fig. 6C). The overall frequency of LT-HSCs was significantly decreased in combined treated mice (Fig. 6D), due to a reduction in GFP^{+} *Calr*-mutant LT-HSCs (Fig. 6E). Similarly, the overall frequency of MkPs and the frequency of GFP^{+} *Calr*-mutant MkPs were significantly reduced in combined treated mice (Fig. 6F+G). However, we found no changes in WBC, and body weight with a significant but stable reduction in hematocrit within

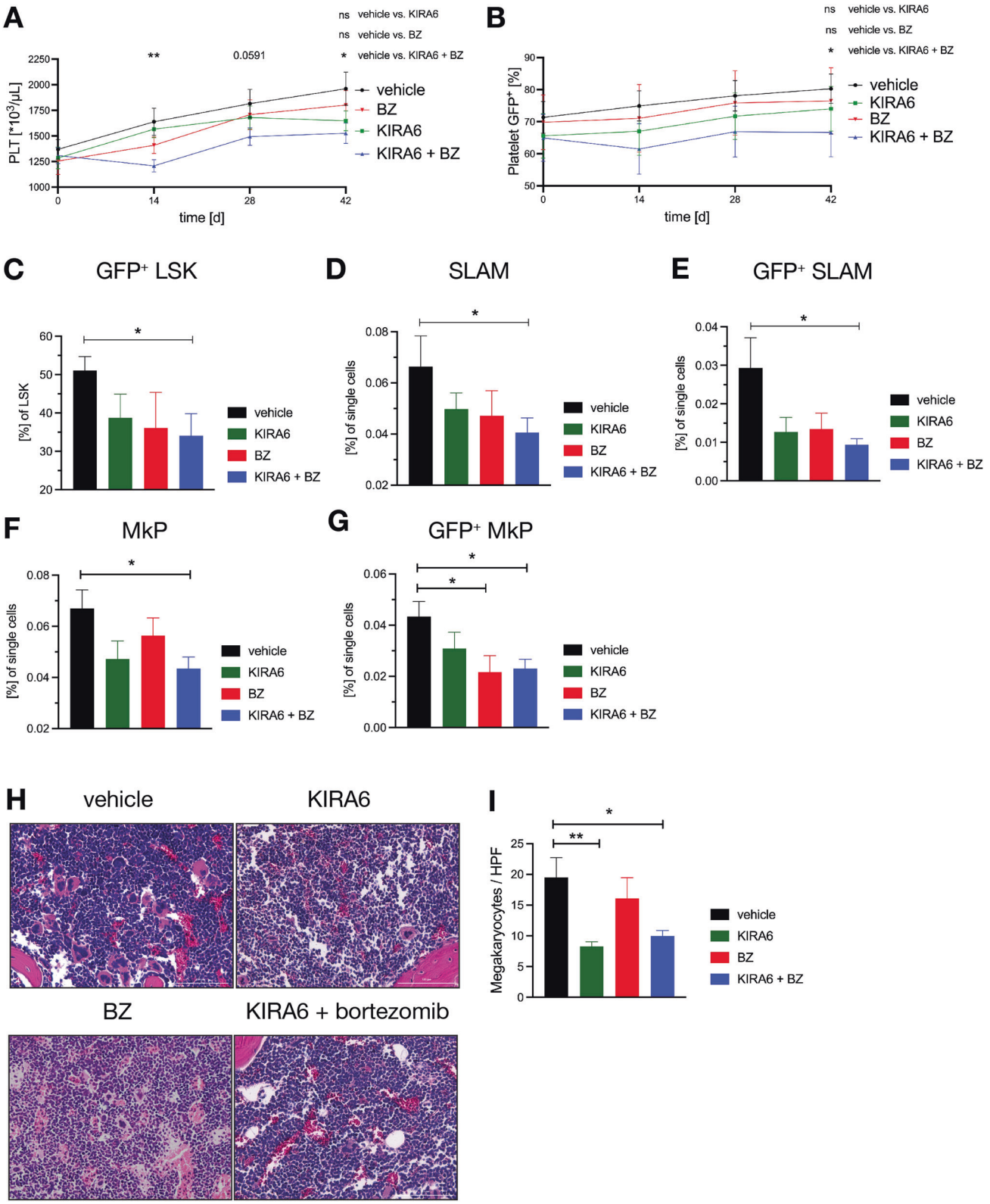

the normal range, indicating the drug combination was well tolerated in our model (Supplementary Fig. 5A–C). We next assessed XBP1s protein levels following treatment. We found a significant reduction in XBP1s frequency in *Calr*-mutant MkP (Supplementary Fig. 5D) in KIRA6 plus bortezomib-treated mice as compared to vehicle-treated mice. Finally, we determined the abundance of megakaryocytes in treated mice using a blinded histopathological assessment. The number of megakaryocytes per high power field was significantly reduced in KIRA6- and KIRA6 plus bortezomib-treated mice as compared to vehicle controls (Fig. 6H+I). Moreover, clustering of megakaryocytes was absent in KIRA6 and KIRA6 plus bortezomib-treated femora. Atypical

Fig. 6 Combined inhibition of the proteasome and the IRE1a-XBP1s axis of the UPR preferentially targets *Calr*$^{\Delta 52/+}$ cells. A Platelet values (PLT) over time of engrafted and pI:pC-induced vehicle, KIRA6, bortezomib, or KIRA6 and bortezomib (BZ)-treated chimeric mice. $n = 7$–14 per group. $n = 2$ donor mice/genotype in two independent experiments. Mean ± SEM. *$p < 0.05$, **$p < 0.01$. **B** GFP chimerism in peripheral blood platelets over time. *$p < 0.05$. **C–G** Immunophenotypic analyses of vehicle, KIRA6, bortezomib, or KIRA6 and bortezomib (BZ)-treated chimeric mice. $n = 7$–14 per group. One-Way ANOVA. Mean ± SEM. * $p < 0.05$. **C** *Calr*$^{\Delta 52/+}$ mutant chimerism (reflected by the percentage of GFP-positive cells) within LSKs. **D** Frequency of total long-term hematopoietic stem cells (SLAM) (**D**) and GFP$^+$ mutant SLAM (**E**) in the bone marrow following six weeks of treatment. Frequency of total megakaryocyte progenitors (MkP) (**F**) and GFP$^+$ mutant MkP (**G**) in the bone marrow following six weeks of treatment. Mean ± SEM. *$p < 0.05$. **H** Histological analysis, hematoxylin and eosin–stained femur sections of vehicle (top left), KIRA6 (top right), bortezomib (bottom left), and KIRA6 + bortezomib-treated (bottom right) mice. (×400 magnification). **I** Average megakaryocyte counts per ten high power fields (HPF) of vehicle, KIRA6, bortezomib, and KIRA6 + bortezomib-treated mice. $n = 6$–11. One-Way ANOVA. Mean ± SEM. *$p < 0.05$, **$p < 0.01$.

megakaryocyte morphology such as the presence of bulbous nuclei, hyperchromatic nuclei, large or small forms was seen in femora in 82% of vehicle-, 43% of KIRA6-, 67% of bortezomib-, and 50% of KIRA6 plus bortezomib-treated mice. (Fig. 6H). Lastly, we performed secondary BM transplantation experiments. We transplanted BM from both treated primary *Calr*-mutant mice (Supplementary Fig. 5) following 28 days of treatment as well as from treated *Calr*-mutant chimeric mice (Fig. 6) following 42 days of treatment. The transplant recipients in both sets of experiments were lethally irradiated WT mice (Supplementary Fig. 6). We did not observe a reduction in *Calr*-mutant donor LT-HSCs in secondary mice that received BM from primary treated *Calr*-mutant mice for any treatment group (Supplementary Fig. 6A–D). Although we found a significant decrease in total SLAM-positive LT-HSCs in secondary mice that received BM from treated *Calr*-mutant chimeric mice in the KIRA6 plus bortezomib treatment group only, there was no significant reduction in GFP + *Calr*-mutant LT−HSCs in this or any treatment group (Supplementary Fig. 6F). In aggregate, the data from the *Calr*-mutant chimeric mouse model indicates that combined inhibition of the proteasome and the ER stress response is more effective in improving the MPN phenotype than either treatment alone, but that combination treatment for 42 days is insufficient to preferentially deplete *Calr*-mutant LT-HSCs as measured by secondary BM transplantation assays.

DISCUSSION

As a calcium-binding ER-resident chaperone protein that regulates protein folding quality control, CALR plays a central role in cellular proteostasis. In MPN, the altered biochemical properties of mutant CALR render it oncogenic, primarily through an aberrant binding interaction with the thrombopoietin receptor, MPL. Here, we explored the consequences of mutant CALR beyond MPL-JAK-STAT signaling, focusing on the cellular response to ER stress and proteasome activity.

Previous studies by us and others have identified the UPR to be transcriptionally upregulated in *CALR*-mutant MPN [13, 26, 27]. Using Genotypes of Transcriptomes, we previously reported that a key node in the UPR, XBP1s, is differentially upregulated in *CALR*-mutant human HSPCs from MPN patients compared to the wild-type counterpart [13]. XBP1s is a basic leucine zipper domain-containing transcription factor that upregulates the expression of UPR target genes, including ER chaperones (e.g., *Dnajb9*, *Dnajb11*, *Pdia3*, and *Dnajc3*), ERAD components, and protein folding enzymes (e.g., *Pdia6*) [10, 28–31]; classes of genes we found to have increased protein expression in *Calr*-mutant primary megakaryocytes (Fig. 1D). In prostate cancer, XBP1s upregulation is one mechanism by which cancer cells overcome ER stress and upregulate pro-survival pathways [32]. XBP1s repression through the inhibition of upstream IRE1a has shown to reduce growth of MYC-driven cancers [32, 33]. A recent study described the successful use of an IRE1a inhibitor in vivo in a retroviral overexpression BM transplant model of mutant CALR-induced MPN [9].

The release of calcium from ER stores by type I *CALR*-mutated cells has been proposed as one mechanism by which the IRE1a-XBP1 branch of the UPR is activated [8, 9]. However, we have previously found transcriptional upregulation of XBP1s in Type II *CALR*-mutated primary MPN samples [13], suggesting that the mechanisms underlying UPR upregulation in *CALR*-mutated MPN cells are not limited to perturbed calcium homeostasis. Given that the ER retention signal (i.e., KDEL) is lost in mutant CALR and secreted mutant CALR protein is detectable in plasma from *CALR*-mutant MPN patients [34] and *Calr*$^{\Delta 52}$ knockin mice [35], it is possible that the overall ER chaperone capacity is compromised in *CALR*-mutated cells, by virtue of less CALR being present in the ER. Since misfolded proteins are shuttled from the ER to the cytosol, followed by ubiquitinylation and degradation by the proteasome via the ERAD pathway, we reasoned that proteasome inhibition (alone or in combination with IRE1 inhibition) might also represent a therapeutic vulnerability in *CALR*-mutant MPN. Importantly, we explored this using a knockin mouse model, where mutant CALR is expressed at physiological levels.

In primary *Calr*$^{\Delta 52/+}$ knockin mice, we found a significant reduction in platelet count in *Calr*$^{\Delta 52}$ mice following treatment with the proteasome inhibitor bortezomib (Fig. 3). Using transplanted chimeric *Calr*$^{\Delta 52}$ mice, we found that although the *Calr*$^{\Delta 52/+}$ mutant myeloid chimerism was reduced upon treatment with bortezomib, platelet counts remained unchanged (Fig. 4). A possible explanation for this is that WT competitor megakaryocytes increased their platelet output in transplanted chimeric mice. Regardless of the reason for an unchanged platelet count, we concluded that single-agent bortezomib was inadequate therapy based on our findings in the *Calr*$^{\Delta 52}$ chimeric model (Fig. 4). We therefore tested combined proteasome/IRE1 inhibition and found superior effects in vivo as compared to either agent alone (Figs. 5+6). This suggests that a dual approach, hitting both the proteasome and the UPR, overwhelms cells with ER stress to induce apoptosis, in heterozygous *Calr*$^{\Delta 52/+}$-expressing MPN cells. Although combined proteasome/IRE1 inhibition reduced megakaryocyte hyperplasia and preferentially targeted *Calr*-mutant megakaryocytes precursor cells and LT-HSCs in the *Calr*$^{\Delta 52}$ chimeric model (Fig. 6), we did not find preferential depletion of *Calr*-mutant LT-HSCs in serial transplantation assays. One potential reason for this is that there is a four-week drug-free period post-transplantation, which may have allowed *Calr*-mutant LT-HSCs to recover. Another possible reason might relate to the duration of the treatment, which was 28 days in primary *Calr*-mutant mice and 42 days in *Calr*-mutant chimeric mice, and in either scenario may represent an inadequate treatment duration for LT-HSC depletion.

Single-agent bortezomib has previously been clinically explored in a phase I/II study for patients with MF [36], based on a pre-clinical study in a thrombopoietin overexpression model of MPN [37]. This clinical trial was performed prior to the discovery of *CALR* mutations in MPN and 12 out of the 13 sequenced patients carried a *JAK2*^{V617F} mutation [36]. In this study, Barosi and colleagues found a mixed response to single-agent bortezomib treatment, concluding that further investigation of the underlying mechanism is necessary to evaluate the use of bortezomib in patients with MPN [36]. The focus

of our study was to investigate *CALR*-mutant MPN, and we have not tested UPR inhibition alone or in combination with bortezomib in *Jak2*^{V617F} MPN mouse models. We have recently reported that UPR pathways are also transcriptionally upregulated in primary MPN platelets isolated from patients harboring a *JAK2*^{V617F} mutation [22]. For this reason, it is possible that *JAK2*-mutant MPN may also be sensitive to combined UPR/proteasome inhibition, but we have not explored this question in this study.

In our study, we investigated the combined inhibition of ER stress and the proteasome, based on a biological rationale, specifically in mutant CALR-driven MPN, and found preferential targeting of the *Calr*-mutant megakaryocyte compartment and the disease-initiating LT-HSCs, although *Calr*-mutant LT-HSCs were not depleted in serial transplantation assays. In summary, we have identified that mechanisms in place to ameliorate ER stress are activated in mutant CALR cells, namely the proteasome and the UPR. Our findings are in line with the known biology of *CALR*-mutant MPN and shed light on upregulated pathways and distinct genetic vulnerabilities with therapeutic potential.

DATA AVAILABILITY

All data generated or analyzed during this study are either included in this published paper [and its supplementary information files] or will be made available upon request.

The long-term hematopoietic stem cell RNA-sequencing data set generated and analyzed during the current study will be made available (GEO accession number in generation). The Genotype of Transcriptome dataset analyzed during the current study is available in the GEO repository, accession ID: GSE117826. Databank URL:

The whole-genome CRISPR depletion screen dataset analyzed during the current study is available in the GEO repository, accession ID: GSE203456

Token: klipmmwivtsnvyn.

REFERENCES

1. Mead AJ, Mullally A. Myeloproliferative neoplasm stem cells. Blood. 2017;129:1607–16.
2. Klampfl T, Gisslinger H, Harutyunyan AS, Nivarthi H, Rumi E, Milosevic JD, et al. Somatic Mutations of Calreticulin in Myeloproliferative Neoplasms. N Engl J Med. 2013;369:2379–90.
3. Nangalia J, Massie CE, Baxter EJ, Nice FL, Gundem G, Wedge DC, et al. Somatic CALR Mutations in Myeloproliferative Neoplasms with Nonmutated JAK2. N Engl J Med. 2013;369:2391–405.
4. Grinfeld J, Nangalia J, Baxter EJ, Wedge DC, Angelopoulos N, Cantrill R, et al. Classification and Personalized Prognosis in Myeloproliferative Neoplasms. N Engl J Med. 2018;379:1416–30.
5. Elf S, Abdelfattah NS, Chen E, Perales-Paton J, Rosen EA, Ko A, et al. Mutant Calreticulin Requires Both Its Mutant C-terminus and the Thrombopoietin Receptor for Oncogenic Transformation. Cancer Disco. 2016;6:368–81.
6. Marty C, Pecquet C, Nivarthi H, El-Khoury M, Chachoua I, Tulliez M, et al. Calreticulin mutants in mice induce an MPL-dependent thrombocytosis with frequent progression to myelofibrosis. Blood. 2016;127:1317–24.
7. Li J, Prins D, Park HJ, Grinfeld J, Gonzalez-Arias C, Loughran S, et al. Mutant calreticulin knock-in mice develop thrombocytosis and myelofibrosis without a stem cell self-renewal advantage. Blood. 2017;131:649–61.
8. Pietra D, Rumi E, Ferretti VV, Buduo CAD, Milanesi C, Cavalloni C, et al. Differential clinical effects of different mutation subtypes in CALR-mutant myeloproliferative neoplasms. Leukemia. 2016;30:431–8.
9. Ibarra J, Elbanna YA, Kurylowicz K, Ciboddo M, Greenbaum HS, Arellano NS, et al. Type 1 but not type 2 calreticulin mutations activate the IRE1a/XBP1 pathway of the unfolded protein response to drive myeloproliferative neoplasmsType 1 CALR mutations activate IRE1a/XBP1 to drive MPNs. Blood Cancer Discov. 2022;3:298–315.
10. Yoshida H, Matsui T, Yamamoto A, Okada T, Mori K. XBP1 mRNA Is Induced by ATF6 and Spliced by IRE1 in Response to ER Stress to Produce a Highly Active Transcription Factor. Cell. 2001;107:881–91.
11. Shen X, Ellis RE, Lee K, Liu C-Y, Yang K, Solomon A, et al. Complementary Signaling Pathways Regulate the Unfolded Protein Response and Are Required for C. elegans Development. Cell. 2001;107:893–903.
12. Calfon M, Zeng H, Urano F, Till JH, Hubbard SR, Harding HP, et al. IRE1 couples endoplasmic reticulum load to secretory capacity by processing the XBP-1 mRNA. Nature. 2002;415:92–6.
13. Nam AS, Kim K-T, Chaligne R, Izzo F, Ang C, Taylor J, et al. Somatic mutations and cell identity linked by Genotyping of Transcriptomes. Nature. 2019;571:355–60.
14. Walter P, Ron D. The Unfolded Protein Response: From Stress Pathway to Homeostatic Regulation. Science. 2011;334:1081–6.
15. Hetz C, Papa FR. The Unfolded Protein Response and Cell Fate Control. Mol Cell. 2018;69:169–81.
16. Harding HP, Calfon M, Urano F, Novoa I, Ron D. Transcriptional and translational control in the mammalian unfolded protein response. Annu Rev Cell Dev Bi. 2002;18:575–99.
17. Szegezdi E, Logue SE, Gorman AM, Samali A. Mediators of endoplasmic reticulum stress-induced apoptosis. Embo Rep. 2006;7:880–5.
18. Sano R, Reed JC. ER stress-induced cell death mechanisms. Biochimica Et Biophysica Acta Bba - Mol Cell Res. 2013;1833:3460–70.
19. Myers SA, Rhoads A, Cocco AR, Peckner R, Haber AL, Schweitzer LD, et al. Streamlined Protocol for Deep Proteomic Profiling of FAC-sorted Cells and Its Application to Freshly Isolated Murine Immune Cells*. Mol Cell Proteom. 2019;18:995–1009.
20. Park S-M, Kang T-I, So J-S. Roles of XBP1s in Transcriptional Regulation of Target. Genes Biomed. 2021;9:791.
21. Han L, Schubert C, Köhler J, Schemionek M, Isfort S, Brümmendorf TH, et al. Calreticulin-mutant proteins induce megakaryocytic signaling to transform hematopoietic cells and undergo accelerated degradation and Golgi-mediated secretion. J Hematol Oncol. 2016;9:45.
22. Jutzi JS, Marneth AE, Ciboddo M, Guerra-Moreno A, Jiménez-Santos MJ, Kosmidou A et al. Whole-genome CRISPR screening identifies N-glycosylation as a genetic and therapeutic vulnerability in CALR-mutant MPN. Blood 2022. https://doi.org/10.1182/blood.2022015629.
23. Bhatt S, Pioso MS, Olesinski EA, Yilma B, Ryan JA, Mashaka T, et al. Reduced Mitochondrial Apoptotic Priming Drives Resistance to BH3 Mimetics in Acute Myeloid Leukemia. Cancer Cell. 2020;38:872–90.e6
24. Chen MZ, Moily NS, Bridgford JL, Wood RJ, Radwan M, Smith TA, et al. A thiol probe for measuring unfolded protein load and proteostasis in cells. Nat Commun. 2017;8:474.
25. Jutzi JS, Kleppe M, Dias J, Staehle HF, Shank K, Teruya-Feldstein J, et al. LSD1 Inhibition Prolongs Survival in Mouse Models of MPN by Selectively Targeting the Disease Clone. Hemasphere. 2018;2:e54.
26. Lau WWY, Hannah R, Green AR, Göttgens B. The JAK-STAT signaling pathway is differentially activated in CALR-positive compared with JAK2V617F-positive ET patients. Blood. 2015;125:1679–81.
27. Prins D, Arias CG, Klampfl T, Grinfeld J, Green AR. Mutant Calreticulin in the Myeloproliferative Neoplasms. Hemasphere. 2020;4:e333.
28. Lee A-H, Iwakoshi NN, Glimcher LH. XBP-1 Regulates a Subset of Endoplasmic Reticulum Resident Chaperone Genes in the Unfolded Protein Response. Mol Cell Biol. 2003;23:7448–59.
29. Yamamoto K, Suzuki N, Wada T, Okada T, Yoshida H, Kaufman RJ, et al. Human HRD1 Promoter Carries a Functional Unfolded Protein Response Element to Which XBP1 but not ATF6 Directly Binds. J Biochem. 2008;144:477–86.
30. Yoshida H, Matsui T, Hosokawa N, Kaufman RJ, Nagata K, Mori K. A Time-Dependent Phase Shift in the Mammalian Unfolded Protein Response. Dev Cell. 2003;4:265–71.
31. Byrd AE, Brewer JW. Intricately Regulated: A Cellular Toolbox for Fine-Tuning XBP1 Expression and Activity. Cells. 2012;1:738–53.
32. Sheng X, Nenseth HZ, Qu S, Kuzu OF, Frahnow T, Simon L, et al. IRE1α-XBP1s pathway promotes prostate cancer by activating c-MYC signaling. Nat Commun. 2019;10:323.
33. Zhao N, Cao J, Xu L, Tang Q, Dobrolecki LE, Lv X, et al. Pharmacological targeting of MYC-regulated IRE1/XBP1 pathway suppresses MYC-driven breast cancer. J Clin Investig. 2018;128:1283–99.
34. Pecquet C, Chachoua I, Roy A, Balligand T, Vertenoeil G, Leroy E, et al. Calreticulin mutants as oncogenic rogue chaperones for TpoR and traffic-defective pathogenic TpoR mutants. Blood. 2019;133:2669–81.
35. Balligand T, Achouri Y, Pecquet C, Gaudray G, Colau D, Hug E, et al. Knock-in of murine Calr del52 induces essential thrombocythemia with slow-rising dominance in mice and reveals key role of Calr exon 9 in cardiac development. Leukemia. 2020;34:510–21.
36. Barosi G, Gattoni E, Guglielmelli P, Campanelli R, Facchetti F, Fisogni S, et al. Phase I/II study of single-agent bortezomib for the treatment of patients with myelofibrosis. Clinical and biological effects of proteasome inhibition. Am J Hematol. 2010;85:616–9.
37. Wagner-Ballon O, Pisani DF, Gastinne T, Tulliez M, Chaligné R, Lacout C, et al. Proteasome inhibitor bortezomib impairs both myelofibrosis and osteosclerosis induced by high thrombopoietin levels in mice. Blood. 2007;110:345–53.

38. Zheng S, Wang W, Aldahdooh J, Malyutina A, Shadbahr T, Tanoli Z et al. SynergyFinder Plus: Toward Better Interpretation and Annotation of Drug Combination Screening Datasets. Genom Proteom Bioinform. 2022. https://doi.org/10.1016/j.gpb.2022.01.004.

ACKNOWLEDGEMENTS

The authors thank Professor Anthony Green (University of Cambridge, UK) for sharing mutant *Calr* knockin mice. The Sysmex veterinary hematology analyzer instrument is a generous loan from Sysmex. We thank Dr. Martha Sola-Visner and her lab members Michael Zhang and Dr. Patricia Davenport (Boston Children's Hospital) for kindly sharing Sysmex equipment for complete blood counts. The authors appreciate the technical support by the BCH Flow lab, namely by Mahnaz Paktinat and Ronald Mathieu as well as by the BWH CCM veterinary staff. JSJ acknowledges funding from the German Research Foundation (DFG, JU 3104/2-1). JSJ is a Special Fellow of The Leukemia & Lymphoma Society (3415-22). AEM receives funding from the US Department of Defense (Horizon Award W81XWH-20-1-0904). BJ is a recipient of the Mildred-Scheel Scholarship from German Cancer Aid (70114570). This work was supported in part by grants from the National Cancer Institute (NCI) Clinical Proteomic Tumor Analysis Consortium grants NIH/NCI U24-CA210986 and NIH/NCI U01 CA214125 (to SAC). YH acknowledges funding support from the Australian Research Council FT210100271. ASN is supported by the Burroughs Wellcome Fund Career Award for Medical Scientists, the National Institutes of Health Director's Early Independence Award (DP5 OD029619-01), and the Starr Cancer Consortium (I15-0026). AM acknowledges funding from NIH NHLBI (R01HL131835), the Gabrielle's Angel Foundation for Cancer Research (GAFCR), and the Starr Cancer Consortium (I15-0026). AM is a Scholar of The Leukemia & Lymphoma Society.

AUTHOR CONTRIBUTIONS

JSJ was responsible for designing the project, conducting the research, extracting and analyzing data, interpreting results, and writing the paper. AEM was responsible for designing the project, conducting the research, extracting and analyzing data, interpreting results, and editing the paper. MJJS was responsible for extracting and analyzing data and interpreting results. JH was responsible for conducting the research and analyzing data. AGM was responsible for conducting the research, extracting and analyzing data, and interpreting results. BR was responsible for conducting the research and analyzing data. SB was responsible for conducting the research and analyzing data. SAM was responsible for conducting the research and analyzing data. SAC was responsible for designing research and supervision. YH was responsible for providing essential material and method support. PvG was responsible for designing research, supervision, and interpreting of results and editing the paper. SEE was responsible for conducting the research extracting and analyzing data, and interpreting results. FAS was responsible for designing research, supervision, and interpreting of results. AN was responsible for designing research, extracting and analyzing data, and interpreting of results and editing the paper. AM was responsible for designing the project, supervision of the project, interpreting results, and writing the paper.

COMPETING INTERESTS

SAC is a member of the scientific advisory boards of Kymera, PTM BioLabs, Seer and PrognomIQ. AM receives research funding from Relay Therapeutics. AM has consulted for Janssen, PharmaEssentia, Actuate, Constellation, Aclaris Cellarity, Morphic, BioMarin, Protagonist and Incyte. AM has received research funding from Janssen and Actuate Therapeutics.

ADDITIONAL INFORMATION

Supplementary information The online version contains supplementary material available at https://doi.org/10.1038/s41375-022-01781-0.

Correspondence and requests for materials should be addressed to Ann Mullally.

Reprints and permission information is available at http://www.nature.com/reprints

Publisher's note Springer Nature remains neutral with regard to jurisdictional claims in published maps and institutional affiliations.